



A ghost-cell immersed boundary method for simulations of heat transfer in compressible flows under different boundary conditions



Kun Luo^a, Zhenya Zhuang^a, Jianren Fan^{a,*}, Nils Erland L. Haugen^b

^aState Key Laboratory of Clean Energy Utilization, Zhejiang University, Hangzhou 310027, PR China

^bSINTEF Energy Research, N-7465 Trondheim, Norway

ARTICLE INFO

Article history:

Received 8 May 2015

Received in revised form 8 September 2015

Accepted 8 September 2015

Available online 26 September 2015

Keywords:

Immersed boundary method

Heat transfer

Robin boundary condition

Compressible flow

ABSTRACT

In this paper we describe the implementation of a ghost-cell immersed boundary method for compressible flow with Dirichlet, Neumann and Robin boundary conditions. A general second-order reconstruction scheme is proposed to enforce the boundary conditions via ghost points. The convergence test shows that the present method has a second-order accuracy for three types of boundary conditions. Laminar flow heat transfer problems are used to test the capability of the present method to handle different boundary conditions with stationary and moving boundaries. The compressible effect on the heat transfer process is then studied to illustrate the advantage and necessity of combining IB methods with a compressible flow solver.

© 2015 Elsevier Ltd. All rights reserved.

1. Introduction

The development of accurate and efficient methods for arbitrarily complex geometries and multiple boundary conditions has been one of the main issues in computational fluid dynamics. The immersed boundary (IB) method has been demonstrated to have the capability of handling complex fluid–structure interaction problems with high efficiency. The advantages of the IB method, such as simplicity in grid generation, savings in computer resources and straightforward parallelization, have expanded its applications in multiphase flow simulations.

The immersed boundary method was first introduced by Peskin to simulate the blood flow around a human heart valve [1]. The main idea of this method is to use a Cartesian grid for fluid flow simulation together with a Lagrangian representation of the immersed boundary. A forcing term is introduced to represent the interaction between the immersed boundary and the fluid, and a discrete Dirac-delta function is used to smooth this singular force on the Euler grid [2]. Since then, numerous modifications and improvements have been made, which are well discussed and categorized in [3–5].

The idea of the ghost cell immersed boundary (GCIB) method is based on the work of Mohd-Yusof [6] and Fadlun et al. [7]. The GCIB method treats the immersed boundary as a sharp interface, and does not require the explicit addition of discrete forces in

the governing equations, thus it can be easily combined with the existing solvers. The boundary condition on the IB is enforced through the “ghost cells”. The variable values of the ghost cells are calculated with the IB boundary conditions and the fluid variables near the boundary. The flow solver senses the presence of the immersed boundary through the extrapolated values at the ghost points [8]. In order to avoid numerical instability caused by the large, negative weighting coefficients in the extrapolation formula, the concept of mirror points lying inside the flow domain is adopted to ensure suitable weighting coefficients in the reconstruction formula. Different interpolation procedures for the mirror point [9] and extrapolation procedures for the ghost point [10,11] can be utilized to obtain a second or even higher order accuracy [12–14]. The GCIB method has shown large potential to handle different fluid–solid interaction problems, including those involving highly complex geometries [15–17] and moving/deforming objects [18–20].

Extension of the immersed boundary method to heat transfer problems has gained its popularity since Kim and Choi [21]. Many efforts have been made to improve the accuracy of thermal boundary condition enforcement and broaden its application. Dirichlet and Neumann type boundary conditions for IB methods have been studied by many researchers [21–26]. While for more complicated boundary conditions, such as Robin and conjugate boundary conditions, the number of available studies are still limited [27–29]. The Robin boundary condition, also known as the mixed Dirichlet–Neumann boundary condition, is important in heat and mass diffusion processes coupled with convection and has been

* Corresponding author. Tel./fax: +86 571 87951764.

E-mail address: fanjr@zju.edu.cn (J. Fan).

used for prescribing thermal or mass fluxes and surface reactions [30–33].

Many fluid dynamic problems of engineering interest involve compressible flows with very different Mach numbers and complex heat/mass transfer processes. There are plenty of parameters that are strongly coupled to each other like density or temperature in a compressible flow. The influence of temperature ratio and Mach number on the flow region has been illustrated by Wang et al. [34] and Sabanca et al. [35]. These results indicate that there is a large difference in the heat transfer phenomena between the compressible flow and the incompressible one, and show the limitation of the incompressible solver for flows with large temperature ratios and high Mach numbers. So far, only a few IB methods are designed for compressible flows [36,37]. Therefore, it is desirable to develop an IB method based on a compressible solver for heat transfer simulation with complex boundary conditions, which is more practical and has a potential to solve chemical reaction problems.

To this end, a general boundary condition treatment, using the ghost-cell immersed boundary method for compressible flows, is developed and validated in the present work. The interaction between immersed bodies and the fluid is expressed by ghost points inside the immersed bodies, and these ghost points ensure that boundary conditions are satisfied precisely on the immersed boundary. Different reconstruction stencils are carried out to maintain the second-order accuracy of the method for different boundary conditions.

The reminder of the present paper is organized as follows. Sections 2 and 3 describe the numerical methodology including the flow solver and the ghost-cell immersed boundary method. In Section 4 the capability of the proposed methodology to handle heat transfer problems with different boundary conditions in compressible flows is verified and validated, including flows with moving interface and medium Mach numbers. Section 5 is devoted to summary and conclusions.

2. Governing equations

The Navier–Stokes equations for a compressible fluid are introduced here. The continuity equation is solved in the form

$$\frac{\partial \rho}{\partial t} + \nabla \cdot (\rho \mathbf{u}) = 0, \tag{1}$$

where ρ is the fluid density, \mathbf{u} is the fluid velocity, t is time.

The momentum equation is written in the form

$$\frac{D\mathbf{u}}{Dt} = \frac{1}{\rho} (-\nabla p + F_{vs}), \tag{2}$$

where p is the pressure, $F_{vs} = \nabla \cdot (2\rho\nu\mathbf{S})$ is the viscous force, ν is the kinematic viscosity, $S_{ij} = \frac{1}{2}(\partial u_i/\partial x_j + \partial u_j/\partial x_i) - \frac{1}{3}\delta_{ij}\nabla \cdot \mathbf{u}$ is the trace-less rate of strain tensor and $D/Dt = \partial/\partial t + \mathbf{u} \cdot \nabla$ is the convective derivative.

The energy equation is

$$\frac{\partial \ln T}{\partial t} = -\mathbf{u} \cdot \nabla \ln T + \frac{1}{\rho c_p T} (\nabla \cdot (k\nabla T) + 2\rho\nu\mathbf{S} \otimes \mathbf{S}), \tag{3}$$

where T is the temperature, c_p is the specific heat at constant pressure and k is the heat conductivity.

The ideal gas equation of state is given by

$$p = \rho RT \tag{4}$$

and can be reduce to

$$p = c_s^2 \rho. \tag{5}$$

for isothermal flow. Here $c_s = \sqrt{\partial p/\partial \rho}$ is the speed of sound.

The solvers of the PENCIL CODE [38] are utilized for the present study. The sixth-order centered finite-difference scheme for spatial derivatives and third-order Runge–Kutta scheme for time advancement are used to solve the above governing equations. In the simulations, the time step is specified as the Courant time step that is calculated based on a number of constraints involving maximum values of velocity, viscosity, and other quantities on the right hand sides of the evolution equations.

3. Ghost-cell compressible immersed boundary (GCCIB) method

In order to impose the boundary condition in such a way that ensures a sharp interface separating the compressible fluid and the solid, a ghost-cell immersed boundary methodology is developed here. The advantage of easy implementation of this method enables us to use the existing solver of the PENCIL CODE. The basic idea of the GCCIB method developed here to handle different types of boundary conditions is based on the work of Haugen et al. [39].

A schematic diagram of the present GCCIB method is shown in Fig. 1. The domain in shadow denotes the solid domain and the rest is the fluid domain. For the sixth-order finite central difference scheme used here, three layers of ghost points (○) are needed to complete the discretization stencils near the boundary. The other grid points inside the solid domain are solid points (■) which are not used in the calculation. At the beginning of the simulations, a detection of the immersed boundary and assignments of ghost points and fluid points are carried out. Then the wall normal direction from each ghost point can be determined. In this study, the mirror points are defined as the points that are normal to the immersed boundary, lying in the fluid domain and have the same distance to the immersed boundary as their corresponding ghost points.

In most situations, the mirror points do not coincide with the grid points. Thus a bilinear interpolation for 2D cases (or tri-linear interpolation for 3D cases) is used to calculate the fluid properties at the mirror points. The bilinear interpolation for a mirror point with four surrounding fluid points can be expressed as

$$\phi(x, y, z) = C_1 x y + C_2 x + C_3 y + C_4. \tag{6}$$

Here ϕ denotes a generic variable at the mirror point. The four unknown coefficients can be determined using the variable values of the four surrounding points

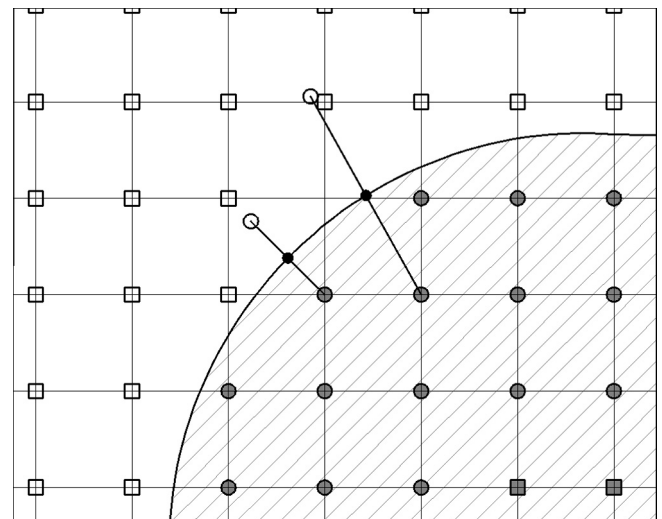


Fig. 1. 2D schematic diagram for the GCCIB method, ghost points (○), mirror points (●), boundary intersection (BI) points (●), fluid points (□) and solid points (■).

$$\{C\} = [V]^{-1}\{\phi\}. \tag{7}$$

where

$$\{C\}^T = \{C_1, C_2, C_3, C_4\} \tag{8}$$

is the vector of the unknown coefficients and

$$\{\phi\}^T = \{\phi_1, \phi_2, \phi_3, \phi_4\} \tag{9}$$

is the vector of the values of the four surrounding grid points. The matrix $[V]$ is expressed as

$$[V] = \begin{pmatrix} x_1y_1 & x_1 & y_1 & 1 \\ x_2y_2 & x_2 & y_2 & 1 \\ x_3y_3 & x_3 & y_3 & 1 \\ x_4y_4 & x_4 & y_4 & 1 \end{pmatrix}. \tag{10}$$

When a ghost point is close to the immersed interface, its mirror point may not have four surrounding fluid points (see in Fig. 2). For such mirror points, we use two fluid points and one boundary intersection point to implement a three-point interpolation stencil [39].

The values of the ghost points can be further calculated with the aid of the mirror points and the given boundary conditions. In this study, the general boundary condition treatment [27] is introduced to represent different boundary conditions:

$$\alpha \left(\frac{\partial \varphi}{\partial n} \right) + \beta \varphi = G. \tag{11}$$

In Eq. (11), φ can be any variable at the immersed interface location, and G is the desired boundary value. The type of the

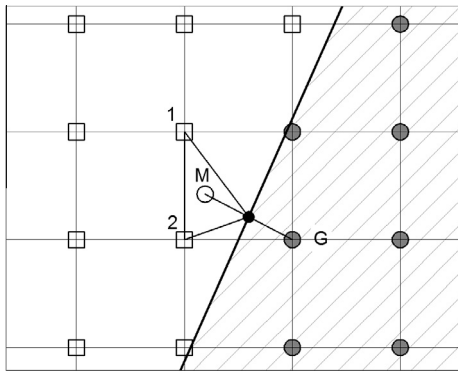


Fig. 2. Interpolation stencil when mirror points are close to the IB. Two fluid points and one BI point are used.

boundary condition is determined by choosing the coefficients α and β . For a Dirichlet type boundary condition, the coefficients of Eq. (11) are set to be $\alpha = 0$ and $\beta = 1$; for a Neumann type boundary condition, the coefficients are $\alpha = 1$ and $\beta = 0$; and for a Robin type boundary condition, both coefficients are non-zero.

3.1. Dirichlet boundary condition

Under the Dirichlet boundary condition, variable values at the immersed boundary are known. A second-order accurate formulation for the value of the variable at the ghost point can be obtained by using the interpolated values at the mirror point together with the given boundary condition at the boundary intersection (BI) point (as shown in Fig. 3(a)), which can be written as

$$\varphi_G = 2\varphi_{BI} - \varphi_M \tag{12}$$

The assumption in the above implementation is that a constant gradient exists between the mirror point and the ghost point.

3.2. Neumann boundary condition

For a Neumann condition specification, the variable gradient at the BI is known instead of the actual value. The most obvious choice in such a case is to use the specified gradient value to compute the value of ghost points as (shown in Fig. 3(a))

$$\varphi_G = \varphi_M + (d_1 + d_0) \left(-\frac{\partial \varphi}{\partial n} \right)_{BI} \tag{13}$$

However, if only one mirror point is used to perform this operation, the numerical accuracy is observed to drop to first order. In order to preserve the second order accuracy, it is necessary to define two probe points along the surface normal direction, as shown in Fig. 3(b), to construct the extrapolation formulation for the ghost point:

$$\varphi_G = \frac{\varphi_1 + \varphi_2}{2} - \frac{(d_0 + d_1)}{2} \left(\frac{\partial \varphi}{\partial n} \right)_{BI} + \frac{d_2 + d_0}{2(d_2 - d_1)} (\varphi_1 - \varphi_2). \tag{14}$$

The position of the probe points are chosen to be $0.7\Delta x$ before and after the mirror point so that the two points are in different grids. When the mirror point is close to the IB, the first probe point may lie inside the solid domain. In this situation, the probe points need to be relocated so that the first probe point is outside the solid domain.

A Neumann boundary condition is often used for the pressure calculation at the ghost location. The pressure gradient in the vicinity of the immersed boundary needs to be zero to fulfill the non-penetration condition and this is implemented through the

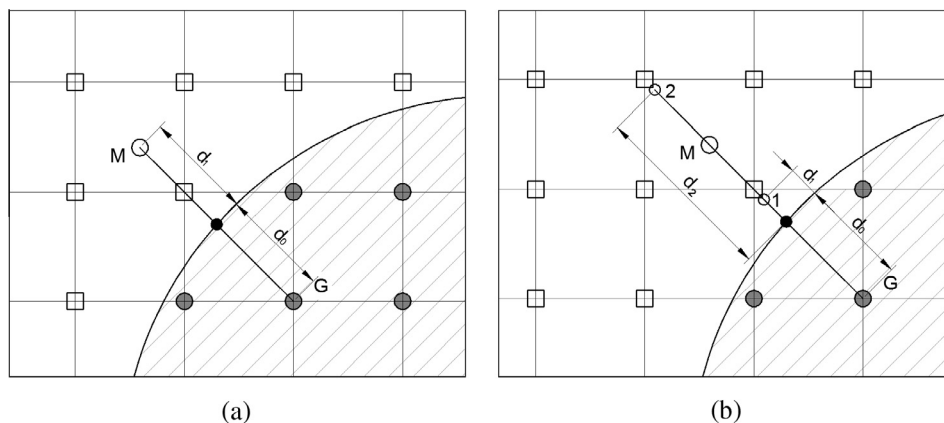


Fig. 3. Extrapolation implementation for (a) Dirichlet boundary condition and (b) Neumann or Robin boundary condition with two probe points.

reconstruction of the density by applying the equation of state. The density values at the ghost points can be obtained by a first-order expression

$$\rho_G = \rho_M \quad (15)$$

for isothermal cases and

$$\rho_G = \rho_M T_M / T_G \quad (16)$$

for non-isothermal cases to ensure $(\frac{\partial \rho}{\partial n})_{BI} = 0$. The second-order formulation, as presented in Eq. (14), can also be used for the ghost point density calculation as

$$\rho_G = \frac{\rho_1 + \rho_2}{2} + \frac{d_2 + d_0}{2(d_2 - d_1)}(\rho_1 - \rho_2) \quad (17)$$

for isothermal cases and

$$\rho_G = \frac{\rho_1 T_1 + \rho_2 T_2}{2T_G} + \frac{d_2 + d_0}{2(d_2 - d_1)} \cdot \frac{\rho_1 T_1 - \rho_2 T_2}{T_G} \quad (18)$$

for non-isothermal cases.

Since the ghost points in the solid object are not obtained from the continuity equation, the mass conservation in the fluid–solid interface is not necessarily fulfilled. Thus, a sufficiently refined grid is usually desired to make the mass conservation violation as low as possible.

3.3. Robin boundary condition

The Robin boundary condition can be seen as a linear combination of the variable value and its gradient at the immersed interface. Here, the value at the immersed interface is given by

$$\varphi_{BI} = \frac{\varphi_G + \varphi_M}{2} \quad (19)$$

while the gradient at the interface is expressed as

$$\left(\frac{\partial \varphi}{\partial n}\right)_{BI} = \frac{1}{d_0 + d_1} \left[\varphi_1 + \varphi_2 - 2T_G + \frac{d_2 + d_0}{d_2 - d_1}(\varphi_1 - \varphi_2) \right] \quad (20)$$

The values at the ghost points can now be calculated by inserting the two equations with Eq. (11).

4. Numerical implementation

4.1. Accuracy examination

During the development of the present GCCIB method, care has been taken to maintain a second-order spatial accuracy in the imposition of boundary conditions on the immersed interface. Thus, one expects that the method will exhibit second-order accuracy at the immersed boundary. The convergence test for flow past a circular cylinder at $Re = 20$ and $Pr = 0.7$ in a domain size of $10D \times 10D$ is carried out to examine the spatial accuracy of the present method. Partially reflecting Navier–Stokes characteristic boundary conditions (NSCBC) [40] are applied at both the inlet and outlet in the streamwise direction, while periodic boundary conditions are used in the spanwise direction. The Mach number is chosen to be 0.01. The cylinder is placed in the center of the domain with a uniform flow, and a solution based on potential flow theory is used as initial condition. The same flow is computed on a series of grids (200×200 , 400×400 and 800×800). We chose a relatively small time step of 3×10^{-6} s and integrate the solution for 10^5 time steps. For a Dirichlet boundary condition, the temperature and the velocity around the cylinder are compared with the desired values. For Neumann and Robin boundary conditions, the results with a highly resolved grid of 1600×1600 are used as a baseline.

Norms of relative errors of variable distributions are indicative of accuracy of the scheme when the grid size changes. Since we mainly care about the accuracy in the vicinity of the IB, the temperature and velocity around the cylinder are used for comparing the results obtained with the different resolutions. Fig. 4 shows the L_2 -norm errors of velocity and temperature at the immersed boundary. The line of Slope 1 and Slope 2 correspond to first and second order accuracy. It is observed that second order convergence is achieved for the velocity and temperature under all different boundary conditions.

4.2. Flow over fixed circular cylinder

In this section, the present ghost-cell compressible immersed boundary method is first validated by simulating isothermal forced convection over a stationary circular cylinder. The domain boundary conditions are the same as those used in Section 4.1. The Mach number is chosen to be 0.01 so that the compressible effect can be neglected and the results can be compared with data from an incompressible flow. A large domain of $20D \times 20D$ is utilized to minimize domain confinement effects and the grid resolution is chosen to be $h = 1/70D$.

Fig. 5(a) and (b) represents the computed streamline for $Re = 20$ and 40. The streamlines around the cylinder are smooth enough, indicating that the present method has successfully captured the flow around the immersed boundary. The surface pressure coefficient is defined as $C_p = \frac{(p - p_\infty)}{1/2 \rho U_\infty^2}$, which is represented in Fig. 5(c) and compared with the results in [41]. The density becomes largest at the front stagnation point and is smallest at the separating points, which corresponds to a variation in pressure coefficient C_p around the cylinder surface. In general, the pressure coefficient C_p at $Re = 20$ and 40 shows good agreement between the present study and the reference data.

The drag and lift coefficients are defined as $C_D = \frac{F_D}{1/2 \rho U_\infty^2 D}$ and $C_L = \frac{F_L}{1/2 \rho U_\infty^2 D}$, respectively, where F_D and F_L are the drag and lift forces. The total force on the cylinder is given by the sum of the pressure and viscous force integrated over the cylinder surface A , which is $F = \int_A PdA + \int_A \tau dA$, where τ is the viscous stress tensor. The total drag force, the length of the recirculation bubble and the Strouhal number are compared with those of other studies

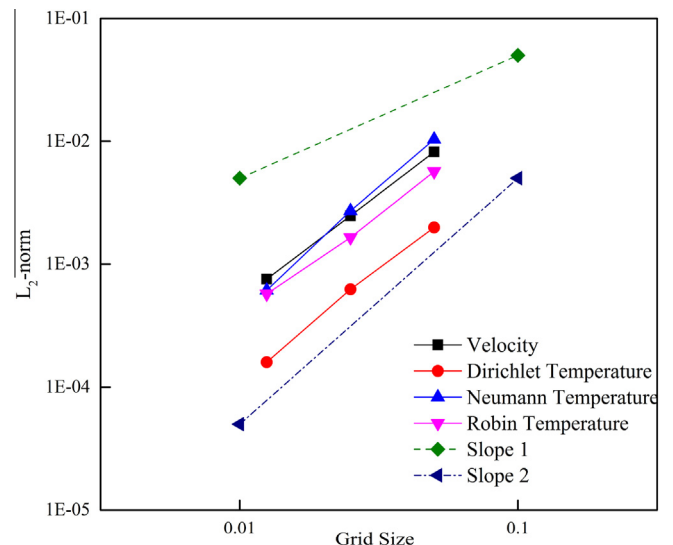


Fig. 4. L_2 -norms computed at various grid levels for application of velocity, and different boundary conditions at the immersed boundary.

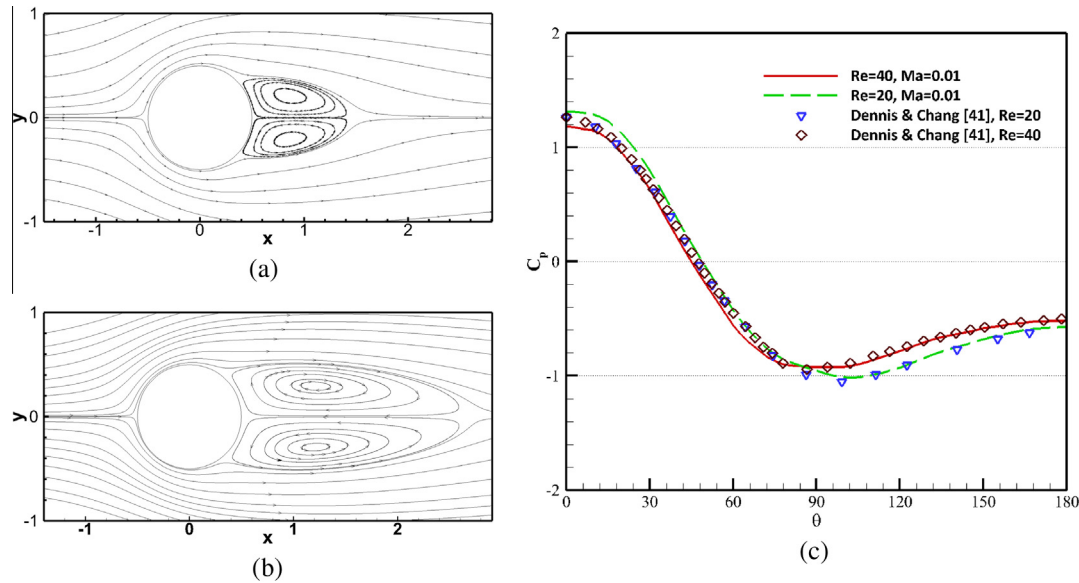


Fig. 5. Computed streamline pattern for (a) $Re = 20$ and (b) $Re = 40$; (c) pressure coefficient for $Re = 20$ and $Re = 40$.

[29,41,42] in Table 1. The results show that the drag coefficient C_D , the Strouhal number Str and the recirculation length L_w are in good agreement with other studies.

4.3. Heat transfer of a fixed cylinder in a free flow with different boundary conditions

The flows and heat transfer over a circular cylinder of unit diameter, at Reynolds numbers $Re = 20$ and 40 and a Prandtl number of $Pr = 0.7$, are investigated in this section in order to validate the code’s capability of handling three types of thermal boundary conditions. Both the temperature ratio and the Mach number are chosen to have moderate values so that the compressible effect can be controlled and the results are comparable with incompressible ones. The influence of the Mach number and the temperature ratio on the heat transfer process will be briefly discussed later.

The domain size, grid resolution and boundary conditions are the same as those described in Section 4.2. The viscosity and heat diffusivity are set to be constant. The local Nusselt number on the boundary interface is defined as

$$Nu_{local} = -\left(\frac{\partial T}{\partial n}\right)_{BI} \frac{D}{T_{BI} - T_0}, \tag{21}$$

where T_{BI} and T_0 are the temperature of the local immersed interface and the temperature of the free flow. The averaged Nusselt number is defined as

$$Nu = \frac{1}{\sum \Delta S} \sum_{surface} Nu_{local} \cdot \Delta S \tag{22}$$

where ΔS is a line segment on the cylinder surface.

The temperature is normalized as

$$\tilde{T} = \frac{T - T_0}{\alpha(\partial T / \partial n)_{BI} + \beta(T_{BI} - T_0)}, \tag{23}$$

in which \tilde{T} means the dimensionless temperature. For Dirichlet boundary condition, the parameters in Eq. (23) can be set as $\alpha = 0$ and $\beta = 1$; for Neumann boundary condition, the parameters can be set as $\alpha = D$ and $\beta = 0$; and for Robin boundary condition, $\alpha = D$ and $\beta = 1$ are set.

Fig. 6 shows the temperature contours for different boundary conditions. The contour increment is $\Delta \tilde{T} = 0.1$. The difference in temperature distribution can clearly be seen by considering the temperature isotherms. The cylinder with Dirichlet boundary condition is most efficient in heat transfer. The dense cluster of isotherms shown in Fig. 6(a) indicates a higher temperature gradient in the flow near the cylinder, especially in the front region. Higher surface temperature and temperature gradient enhance the heat transfer process. While for the cylinder with Neumann boundary condition, the restriction on temperature gradient over the cylinder surface suppress the heat transfer process, and a relatively low temperature in the flow around the cylinder is then as expected. For the Robin boundary condition, the heat transfer process is even worse, since the temperature gradient is related to the local temperature, which means that the temperature gradient will decrease when the flow goes downstream and the fluid temperature will be even lower than that obtained with the Neumann boundary condition.

The local Nusselt number and temperature distribution obtained with the different boundary conditions for $Re = 20$ and $Pr = 0.7$ are shown in Fig. 7. The average Nusselt numbers under the three types of boundary conditions for both $Re = 20$ and $Re = 40$ are shown in Table 2. The present results agree well with those of previous studies [29,43], which demonstrates the capability of the present ghost-cell method for handling the three types of different boundary conditions. Lower cylinder surface temperature can be observed under Neumann and Robin boundary conditions, which is consistent with the temperature distribution shown in Fig. 6.

4.4. Flow past an in-line oscillating cylinder with heat transfer

A primary attempt to apply the present GCCIB method to a moving body is made in this section. The case of free flow past an in-line oscillating cylinder in a free stream at $Re = 100$ and $Pr = 0.7$ with

Table 1 Comparison of drag coefficient C_D , recirculation length L_w and Strouhal number Str with other previous studies.

	$Re = 20$		$Re = 40$		$Re = 100$	
	C_D	L_w	C_D	L_w	C_D	Str
Present	2.117	0.92	1.578	2.17	1.337	0.169
Tritton [42] (exp)	2.09	-	1.58	-	1.25	-
Dennis and Chang [41]	2.045	0.99	1.522	2.35	-	-
Pan [29]	2.039	0.914	1.522	2.258	1.336	0.164

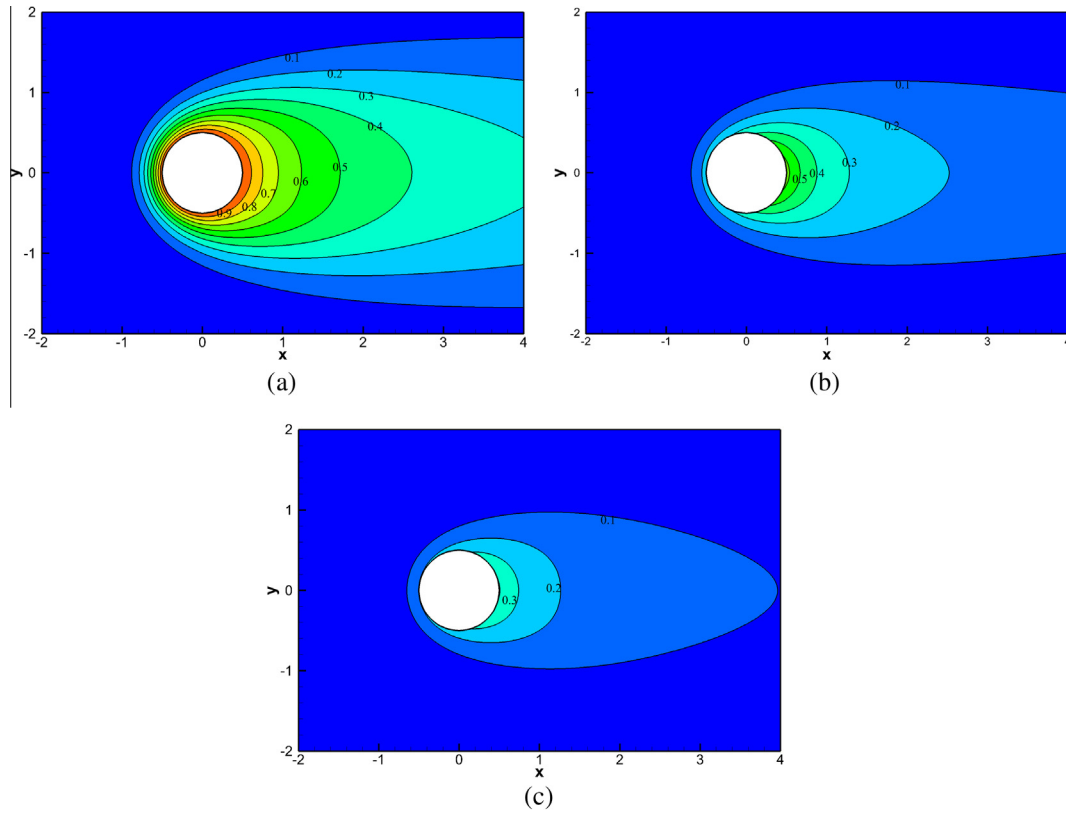


Fig. 6. Temperature contours for (a) Dirichlet boundary condition, (b) Neumann boundary condition and (c) Robin boundary condition.

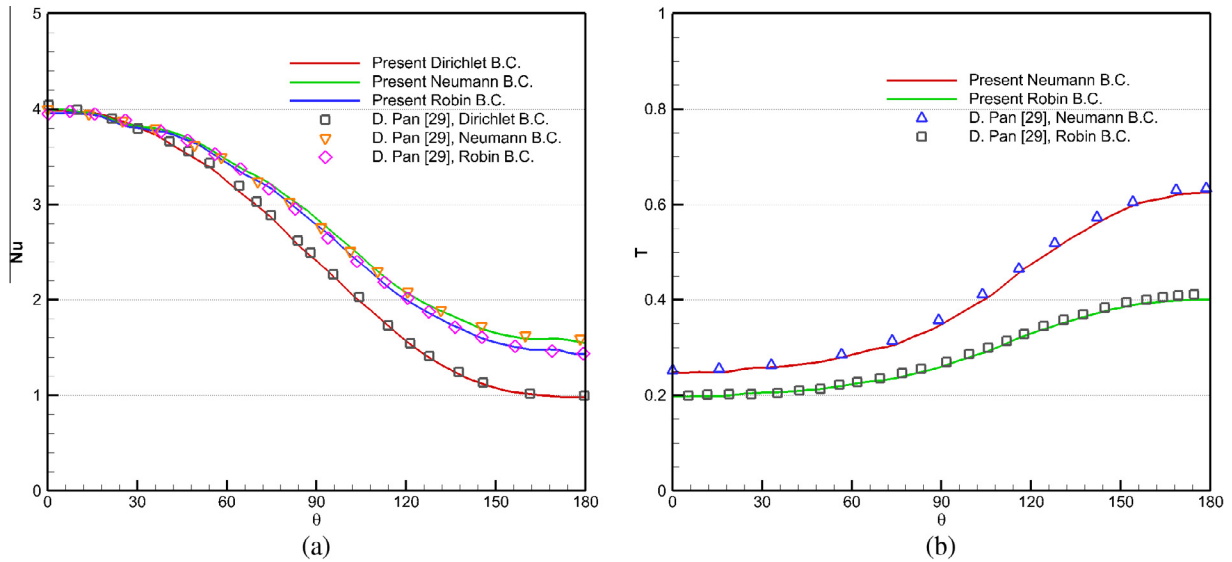


Fig. 7. (a) Local Nusselt number distribution of three types of boundary conditions; (b) local temperature distribution of Neumann and Robin boundary conditions.

Table 2
Averaged Nusselt number over the cylinder surface under different boundary condition, $Re = 20$ and 40 .

Methods	Re, Pr	Nu (Dirichlet)	Nu (Neumann)	Nu (Robin)
Present	20, 0.7	2.4336	2.7850	2.7221
Pan [29]	20, 0.71	2.4553	2.7739	2.7202
Bharti et al. [43]	20, 0.7	2.4653	2.7788	-
Present	40, 0.7	3.2466	3.7950	3.6532
Pan [29]	40, 0.71	3.2653	3.7703	3.7078
Bharti et al. [43]	40, 0.7	3.2825	3.7755	-

heat transfer is used for a test. According to the study of Hurlbut et al. [44], choosing an oscillation frequency of the cylinder of approximately twice the Strouhal frequency of the vortex shedding causes a phase-locking, which can effectively increase the average drag coefficient $C_{D,mean}$ and maximum lift coefficient $C_{L,max}$. The computational domain in the present simulation is chosen to be $20D \times 16D$ and the grid size near the immersed boundary is $h = D/75$. The cylinder is located in the center of the domain. The Mach number in the present study is 0.025. The motion of the cylinder is now described by setting its horizontal position to

$$X_c(t) = A \sin(2\pi f_c t) \tag{24}$$

The amplitude A is set to be $A/D = 0.14$. The oscillation frequency is chosen to be $f_c/f_0 = 2$, where f_0 is the frequency of natural vortex shedding of a corresponding stationary cylinder. Neglecting the heat radiation, the heat transfer process between the cylinder and the ambient fluid is usually considered as

$$h(T_{IB} - T_0) = -\lambda_s \left(\frac{\partial T}{\partial n} \right)_{IB}, \tag{25}$$

where h means the convective heat transfer coefficient and λ_s is the heat conductivity of the cylinder. Thus, the thermal boundary condition of the cylinder is set as the Robin type boundary condition.

Fig. 8 shows the instantaneous vorticity and temperature contours at five instants of time within one vortex shedding period. The synchronization of vortex shedding and temperature field with cylinder movement is clearly observed by comparing Fig. 8(a) with Fig. 8(e), and Fig. 8(f) with Fig. 8(j). This indicates that the present method is able to successfully capture the lock-in phenomenon of the flow and thermal fields.

To further investigate the influence of synchronization, the variation of the drag and lift coefficients, together with the Nusselt number, were recorded over one period, as shown in Fig. 9. Time-averaged drag coefficient, Nusselt number and maximum lift coefficient are shown in Table 3 and compared with corresponding data from the literature. When the cylinder is oscillating at a

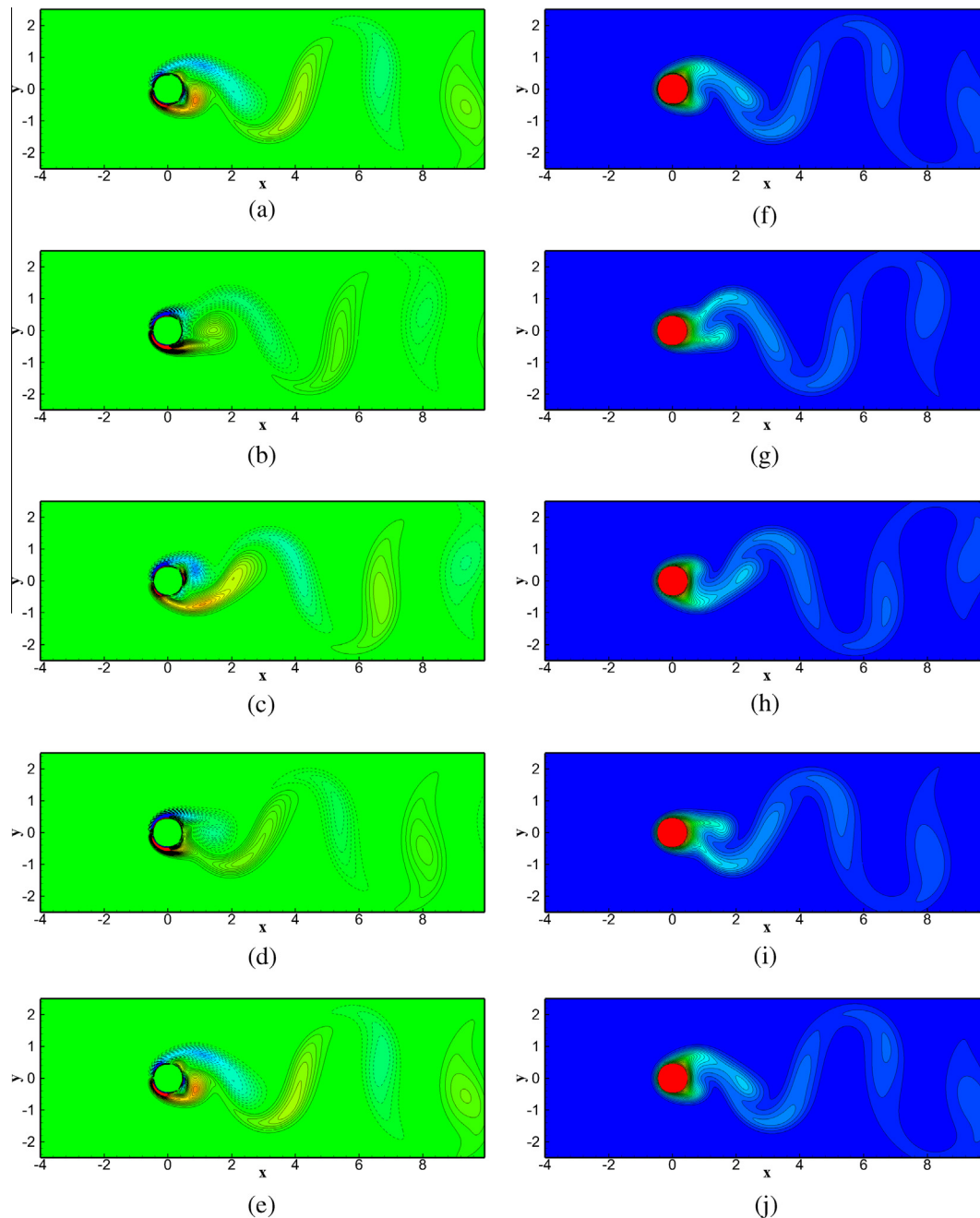


Fig. 8. Vorticity contours (a)–(e) and isotherms (f)–(j) for in-line oscillating cylinder at $Re = 100$ when $f_c/f_0 = 2.0$. (a) and (f): 0.0T; (b) and (g): 0.25T; (c) and (h): 0.5T; (d) and (i): 0.75T; (e) and (j): 1.0T.

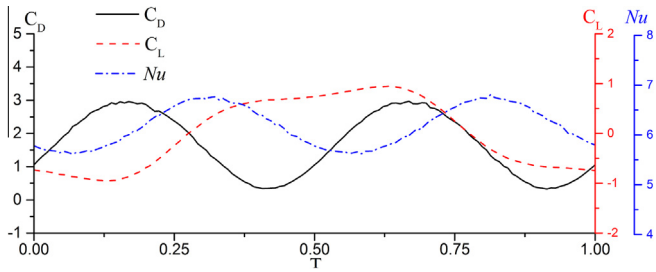


Fig. 9. Computed C_D , C_L , and Nu variation for in-line oscillating cylinder with Robin type thermal boundary condition when lock-in happens ($Re = 100, f_c/f_0 = 2$).

Table 3
Comparison of lift and drag coefficients of in-line oscillating cylinder in a free stream at $Re = 100$.

	f_c/f_0	$C_{D,mean}$	$C_{L,max}$	Nusselt
Present	0	1.3773	0.3303	5.9161
	2	1.6834	0.9516	6.6194
Pan [29]	0	1.336	0.3238	5.9255
Hurlbut et al. [44]	0	1.41	0.31	–
	2	1.68	0.95	–
Orley et al. [45]	0	1.39	0.33	–
	2	1.73	0.93	–

lock-in frequency, there is a noticeable increase in the amplitude of the drag and lift forces, and an increase in the Nu number. The C_D and Nu change periodically with a frequency of f_c , while the lift C_L changes with a frequency of f_0 . Time-averaged overall Nusselt number and the drag coefficient also increase when the lock-in occurs. A good agreement is observed when comparing with those in literature, which demonstrates that the present method can capture the important practical flow and thermal properties very well for moving-body problems.

4.5. The compressible effect on heat transfer

As shown in the governing equations and mentioned in the Introduction, there are plenty of parameters that are strongly coupled to each other in a compressible flow such as density, temperature, and pressure, which makes it much more complicated than incompressible flows. The Reynolds and Prandtl numbers alone are not enough to define the flow characteristics in a compressible flow. More parameters, like Mach number and temperature ratio, have to be included in order to describe the flow phenomena. In Section 4.3, the investigation of the heat transfer process is limited to a very small Mach number of 0.01 to control the compressible effect for code validation. In the current section, the primary purpose is to test the capability of the present method to describe flow and thermal phenomena in higher Mach number flows. The effects of Mach number on the flow patterns and parameters such as the pressure, drag coefficients and Nusselt numbers are also discussed.

The computational domain in the present simulation is chosen to be $20D \times 16D$ and the grid size near the immersed boundary is $h = D/75$. The cylinder, with the Robin boundary condition, is located in the center of the domain. The Mach number in this study is 0.05, 0.1, 0.2 and 0.3. The temperature ratio between the solid and the ambient fluid is defined as $T^* = (\alpha \frac{\partial T}{\partial n} + \beta T)/T_0$ and is set to $T^* = 1.1$. The viscosity and the thermal diffusivity are set to be constant.

The influence of Mach number on flow parameters like drag coefficient and Strouhal number is shown in Fig. 10. The increase of the Mach number causes an increase in both the drag coefficient and the vortex shedding frequency. The physical interpretation of

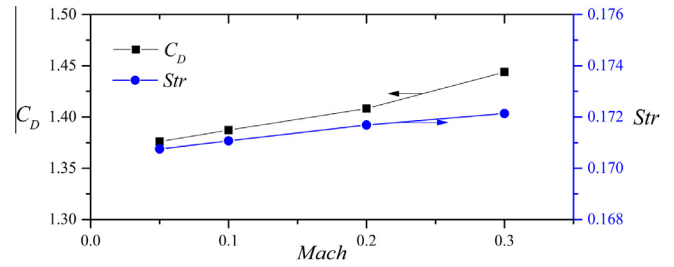


Fig. 10. Influence of Mach number on drag coefficient and Strouhal number at constant temperature ratio of $T^* = 1.1$.

this phenomenon is that with the increase of the Mach number the fluid near the cylinder is compressed accordingly. Such a compressible effect causes a temperature raise (see Fig. 12(a)) as well as an increase in the density near the cylinder, especially in the front region. According to the equation of state, the value of the pressure in front of the object increase faster than the pressure behind it, and an increase in the pressure component of the drag force is therefore expected. Besides, the increase of density may also increase the viscous force around the cylinder, which also contributes to the raise of the drag coefficient. The effect of compressibility on the Strouhal number is consistent with the results of [35]. As the Mach number increase, the Strouhal number also increases slightly.

The influence of the Mach number on the heat transfer process is observed by considering the temperature contours for different Mach numbers shown in Fig. 11. As can be seen, the Mach number

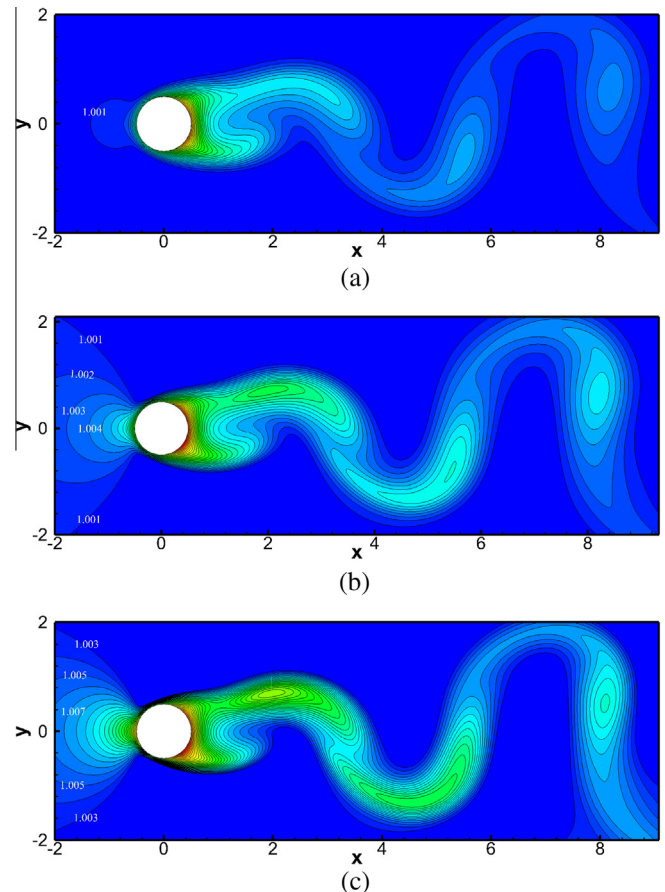


Fig. 11. Temperature contours of a cylinder in a free stream with Robin boundary condition at different Mach numbers. (a) $Ma = 0.1$; (b) $Ma = 0.2$; (c) $Ma = 0.3$.

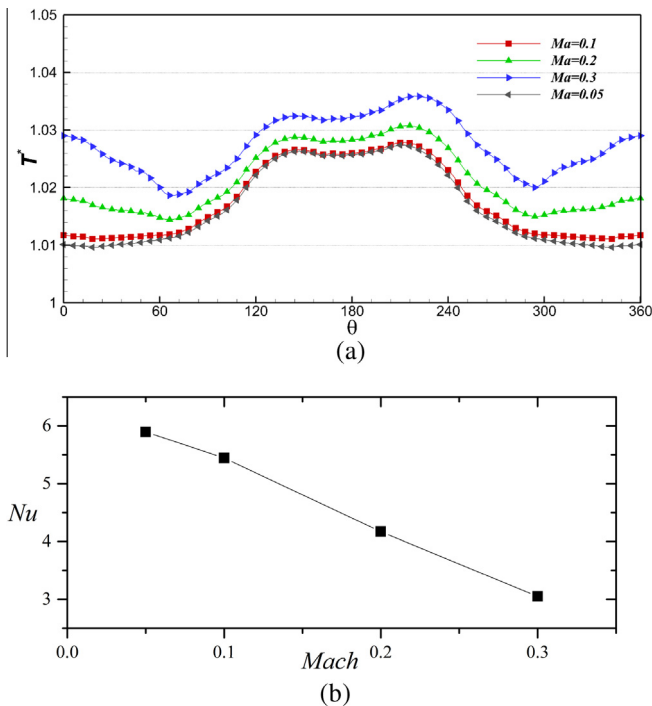


Fig. 12. (a) Instantaneous local temperature values around the cylinder surface at the phase position of Fig. 11 in different Mach numbers; (b) averaged Nusselt number variation due to the change of Mach number.

effect increases the fluid temperature in the vicinity of cylinder surface, especially so in the front part. Even the fluid in the upstream region is influenced by this effect. As the Mach number increases, the fluid temperature near the surface gets higher and the isotherms go further upstream. Such a raise of fluid temperature highly restricts the solid–fluid heat transfer process and causes a decrease in the average Nusselt number. As shown in Fig. 12(b), when the Mach number increases from 0.05 to 0.3, the Nu number has decreased almost 48% and most of this decrease comes from the front region.

Although the Mach number in the present study is kept moderate ($Ma < 0.3$), its influence on flow and thermal patterns is still obvious. An even more prominent influence can be expected for higher Mach numbers. The combination of the present IB method and the compressible solver allows us to investigate multiphase flow problems with complex boundary conditions, large Mach numbers, and large temperature ratios.

5. Conclusion

In the current work we have presented a second-order reconstruction scheme for the ghost-cell immersed boundary method to handle Dirichlet, Neumann and Robin type heat transfer problems in compressible flows. The present method shows second-order accuracy for three types of boundary conditions and has been validated by simulating the laminar heat transfer process of a circular cylinder in a free stream. A primary attempt to apply the present IB method on the simulation of moving boundaries was also made. A validation study for an in-line oscillating cylinder in a free stream shows that the present method successfully captures the lock-in phenomena in the flow and thermal field. Finally, a study of the compressible effect in the heat transfer process is carried out to illustrate the capability of the method for relatively high Ma number flows, as well as the advantage of combining IB methods with a compressible flow solver. Further

improvements, like the inclusion of non-spherical geometries and multiple objects interaction, will be straightforward.

Conflict of interest

None declared.

Acknowledgement

Financially support by the National Natural Science Foundation of China (Nos. 51222602, 51390490) is acknowledged. This work is also partially supported from the Zhejiang Provincial Natural Science Foundation (No. LR12E06001) and the Fundamental Research Funds for the Central Universities.

References

- [1] C.S. Peskin, Flow patterns around heart valves: a numerical method, *J. Comput. Phys.* 10 (2) (1972) 252–271.
- [2] C.S. Pekin, The immersed boundary method, *Acta Numer.* 11 (2002) 479–517.
- [3] R. Mittal, G. Iaccarino, Immersed boundary methods, *Annu. Rev. Fluid Mech.* 37 (2005) 239–261.
- [4] S. Haeri, J.S. Shrimpton, On the application of immersed boundary, fictitious domain and body-conformal mesh methods to many particle multiphase flows, *Int. J. Multiphase Flow* 40 (2012) 38–55.
- [5] F. Sotiropoulos, X. Yang, Immersed boundary methods for simulating fluid–structure interaction, *Prog. Aerosp. Sci.* 65 (2014) 1–21.
- [6] J. Mohd-Yusof, Combined Immersed Boundary/B-spline Methods for Simulation of Flow in Complex Geometries, CTR Annual Research Briefs, NASA Ames/Stanford University, 1997.
- [7] E.A. Fadlun, R. Verzicco, P. Orlandi, J. Mohd-Yusof, Combined immersed-boundary finite-difference methods for three-dimensional complex flow simulations, *J. Comput. Phys.* 161 (1) (2000) 35–60.
- [8] S. Majumdar, G. Iaccarino, P. Durbin, RANS solvers with adaptive structured boundary non-conforming grids, *Ann. Res. Briefs* (2001) 353–366.
- [9] Y. Tseng, J.H. Ferziger, A ghost-cell immersed boundary method for flow in complex geometry, *J. Comput. Phys.* 192 (2) (2003) 593–623.
- [10] H. Ding, C. Shu, Q.D. Cai, Applications of stencil-adaptive finite difference method to incompressible viscous flows with curved boundary, *Comput. Fluids* 36 (4) (2007) 786–793.
- [11] O. Hu, N. Zhao, J.M. Liu, A ghost cell method for turbulent compressible viscous flows on adaptive cartesian grids, *Proc. Eng.* 67 (2013) 241–249.
- [12] H. Luo, R. Mittal, X. Zheng, S.A. Bielamowicz, R.J. Walsh, J.K. Hahn, An immersed-boundary method for flow–structure interaction in biological systems with application to phonation, *J. Comput. Phys.* 227 (22) (2008) 9303–9332.
- [13] J.H. Seo, R. Mittal, A high-order immersed boundary method for acoustic wave scattering and low-Mach number flow-induced sound in complex geometries, *J. Comput. Phys.* 230 (4) (2011) 1000–1019.
- [14] J. Xia, K. Luo, J. Fan, A ghost-cell based high-order immersed boundary method for inter-phase heat transfer simulation, *Int. J. Heat Mass Transfer* 75 (2014) 302–312.
- [15] R. Mittal, H. Dong, M. Bozkurtas, F.M. Najjar, A. Vargas, A. von Loebbecke, A versatile sharp interface immersed boundary method for incompressible flows with complex boundaries, *J. Comput. Phys.* 227 (10) (2008) 4825–4852.
- [16] P.A. Berthelsen, O.M. Faltinsen, A local directional ghost cell approach for incompressible viscous flow problems with irregular boundaries, *J. Comput. Phys.* 227 (9) (2008) 4354–4397.
- [17] R. Ghias, R. Mittal, H. Dong, A sharp interface immersed boundary method for compressible viscous flows, *J. Comput. Phys.* 225 (1) (2007) 528–553.
- [18] A. Gilmanov, F. Sotiropoulos, A hybrid Cartesian/immersed boundary method for simulating flows with 3D, geometrically complex, moving bodies, *J. Comput. Phys.* 207 (2) (2005) 457–492.
- [19] A. Gilmanov, S. Acharya, A computational strategy for simulating heat transfer and flow past deformable objects, *Int. J. Heat Mass Transfer* 51 (17–18) (2008) 4415–4426.
- [20] M. Shrivastava, A. Agrawal, A. Sharma, A novel level set-based immersed-boundary method for CFD simulation of moving-boundary problems, *Numer. Heat Transfer Part B Fundam.* 63 (4) (2013) 304–326.
- [21] H.C. Jungwoo Kim, An immersed-boundary finite-volume method for simulation of heat transfer in complex geometries, *KSME Int. J.* 18 (6) (2004) 1026–1035.
- [22] N. Zhang, Z.C. Zheng, S. Eckels, Study of heat-transfer on the surface of a circular cylinder in flow using an immersed-boundary method, *Int. J. Heat Fluid Flow* 29 (6) (2008) 1558–1566.
- [23] W. Ren, C. Shu, W. Yang, An efficient immersed boundary method for thermal flow problems with heat flux boundary conditions, *Int. J. Heat Mass Transfer* 64 (2013) 694–705.
- [24] I. Paul, K. Arul Prakash, S. Vengadesan, Forced convective heat transfer from unconfined isothermal and isoflux elliptic cylinders, *Numer. Heat Transfer Part A Appl.* 64 (8) (2013) 648–675.

- [25] D. Pan, A simple and accurate ghost cell method for the computation of incompressible flows over immersed bodies with heat transfer, *Numer. Heat Transfer Part B Fundam.* 58 (1) (2010) 17–39.
- [26] J.R. Pacheco, A. Pacheco-Vega, T. Rodic, R.E. Peck, Numerical simulations of heat transfer and fluid flow problems using an immersed-boundary finite-volume method on nonstaggered grids, *Numer. Heat Transfer Part B Fundam.* 48 (1) (2005) 1–24.
- [27] G.S. Barozzi, C. Bussi, M.A. Corticelli, A fast Cartesian scheme for unsteady heat diffusion on irregular domains, *Numer. Heat Transfer Part B Fundam.* 46 (1) (2004) 59–77.
- [28] A. Pacheco-Vega, J.R. Pacheco, T. Rodic, A general scheme for the boundary conditions in convective and diffusive heat transfer with immersed boundary methods, *Trans. Am. Soc. Mech. Eng. J. Heat Transfer* 129 (11) (2007) 1506.
- [29] D. Pan, A general boundary condition treatment in immersed boundary methods for incompressible Navier–Stokes equations with heat transfer, *Numer. Heat Transfer Part B Fundam.* 61 (4) (2012) 279–297.
- [30] C.G. Bell, H.M. Byrne, J.P. Whiteley, S.L. Waters, Heat or mass transfer at low Péclet number for Brinkman and Darcy flow round a sphere, *Int. J. Heat Mass Transfer* 68 (2014) 247–258.
- [31] Q. Hussain, T. Hayat, S. Asghar, H.H. Alsulami, Mixed convective peristaltic transport in a vertical channel with Robin's condition, *J. Braz. Soc. Mech. Sci. Eng.* 36 (4) (2014) 681–695.
- [32] E.M. Ryan, A.M. Tartakovsky, C. Amon, A novel method for modeling Neumann and Robin boundary conditions in smoothed particle hydrodynamics, *Comput. Phys. Commun.* 181 (12) (2010) 2008–2023.
- [33] Z. Deng, J. Liu, Modeling of multidimensional freezing problem during cryosurgery by the dual reciprocity boundary element method, *Eng. Anal. Boundary Elem.* 28 (2) (2004) 97–108.
- [34] A. Wang, Z. Trávníček, K. Chia, On the relationship of effective Reynolds number and Strouhal number for the laminar vortex shedding of a heated circular cylinder, *Phys. Fluids* 12 (6) (2000) 1401.
- [35] M. Sabanca, F. Durst, Flows past a tiny circular cylinder at high temperature ratios and slight compressible effects on the vortex shedding, *Phys. Fluids* 15 (7) (2003) 1821.
- [36] P. De Palma, M.D. de Tullio, G. Pascazio, M. Napolitano, An immersed-boundary method for compressible viscous flows, *Comput. Fluids* 35 (7) (2006) 693–702.
- [37] M.D. de Tullio, P. De Palma, G. Iaccarino, G. Pascazio, M. Napolitano, An immersed boundary method for compressible flows using local grid refinement, *J. Comput. Phys.* 225 (2) (2007) 2098–2117.
- [38] <https://code.google.com/p/pencil-code/>.
- [39] N.E.L. Haugen, S. Kragset, Particle impact on a cylinder in a crossflow as function of Stokes and Reynolds numbers, *J. Fluid Mech.* 661 (2010) 239–261.
- [40] T.J. Poinso, S.K. Lelef, Boundary conditions for direct simulations of compressible viscous flows, *J. Comput. Phys.* 101 (1) (1992) 104–129.
- [41] S.C.R. Dennis, G. Chang, Numerical solutions for steady flow past a circular cylinder at Reynolds numbers up to 100, *J. Fluid Mech.* 42 (3) (1970) 471–489.
- [42] D.J. Tritton, Experiments on the flow past a circular cylinder at low Reynolds numbers, *J. Fluid Mech.* 6 (4) (1959) 547–567.
- [43] R.P. Bharti, R.P. Chhabra, V. Eswaran, A numerical study of the steady forced convection heat transfer from an unconfined circular cylinder, *Heat Mass Transfer* 43 (7) (2007) 639–648.
- [44] S.E. Hurlbut, M.L. Spaulding, F.M. White, Numerical solution for laminar two dimensional flow about a cylinder oscillating in a uniform stream, *J. Fluids Eng.* 104 (2) (1982) 214–220.
- [45] F. Örley, V. Pasquariello, S. Hickel, N.A. Adams, Cut-element based immersed boundary method for moving geometries in compressible liquid flows with cavitation, *J. Comput. Phys.* (2014).